Interaction potential, transport properties, and velocity distributions of Na$^+$ ions in Ne

P. P. Ong and M. J. Hogan

Physics Department, National University of Singapore, Kent Ridge, Singapore 0511, Republic of Singapore

K. Y. Lam

*Mechanical and Production Engineering Department, National University of Singapore,
Kent Ridge, Singapore 0511, Republic of Singapore*

L. A. Viehland

Parks College of Saint Louis University, Cahokia, Illinois 62206

Comparisons of experimentally measured transport properties with values determined from calculations based on three-temperature-kinetic theory, on bi-Maxwellian kinetic theory, and on Monte Carlo simulations have established that the Na$^+$-Ne interaction potential of Koutselos, Mason, and Viehland [J. Chem. Phys. **93**, 7125 (1990)] is a close approximation to the true potential. (In the bi-Maxwellian approach, the ions are modeled in first-approximation as a large fraction that behaves according to a low-temperature Maxwell distribution and a small fraction that follows one of higher temperature; the true distribution is computed from these by a weighted-residual method.) This potential was then used to compute velocity distribution functions of Na$^+$ ions in room-temperature Ne at widely different average ion energies. The skewness of the distributions in the direction of the electric field initially increased rapidly with increasing energy, and then slowly decreased, as did the excess kurtosis both parallel and perpendicular to the electric-field direction. It was clearly established that there is correlation between the perpendicular and parallel velocity-component distribution functions and that the correlation increases with increasing average ion energy.

PACS number(s): 51.50.+v, 34.20.Cf, 52.25.Fi

INTRODUCTION

In previous work [1–4] with potassium-ion–rare-gas systems, it was found that measured transport data were well represented by the interaction potentials of Koutselos, Mason, and Viehland (KMV) [5]. The purpose of this paper is to show that the KMV potential for Na$^+$-Ne accurately reproduces the available transport data, and then to compute from this potential the velocity distribution functions (VDF's) for a Na$^+$ swarm in Ne gas at widely different average ion energies.

Knowledge about VDF's is of fundamental importance in many areas [6(a)]. An application of potential significance which was recently highlighted [7] is in the development of a vacuum uv ion excimer laser based on the reaction

$$AR^+ \longrightarrow A^+R + h\nu \, , \tag{1}$$

in which the alkali-metal-ion (A^+)–rare-gas-neutral (R) pair provides the final, deenergized, molecular-transition states from the initial, energetic, excimerlike states. Information about VDF's is particularly important for the analysis of flow-drift and drift-tube measurements of rate coefficients for ion-molecule reactions where there is an energy threshold [8]. Additionally, a well-represented VDF would also provide insightful guidance on the choice of a basis function needed in solving the Boltzmann equation such as by the velocity moments

method. Unfortunately, both our theoretical and experimental knowledge of these distributions is still quite limited.

Theoretically derived functional forms [9,10] for ion-velocity distributions are not supported by experimental measurements [11] and sometimes give unacceptable imaginary results when solved with experimentally determined parameters. On the other hand, experimental measurements using retarding-potential-difference methods can, under certain conditions, be subject to important errors caused by distortions of the boundary layers of both the electric potential [12] and the pressure at the end of the drift tube. The recent technique [13,14] of deducing the velocity distribution in a chosen direction from laser-induced fluorescence (LIF) measurements of the Doppler shift due to ionic motion appears promising. However, it has yet to be applied to closed-shell ion-atom systems, where its accuracy can be verified, because of the limited wavelength ranges of available single-mode cw tunable lasers.

The procedure followed here for the determination of ion-velocity distributions starts with an interaction potential. Whether this potential has been obtained from *ab initio* or approximate quantum calculations, from direct inversion of equilibrium, spectroscopic, scattering, or transport data, or from semiempirical (as in the case of the KMV potential) or corresponding-states arguments, the first task is to establish its accuracy. This is done by comparing properties calculated from the potential to experimental values of transport properties. These calcula-

tions are based on three-temperature (3T) kinetic theory [15], on bi-Maxwellian (BM) kinetic theory [16], and on Monte Carlo simulations (MCS) [1,2]. Once the potential is known to be accurate, it is possible to extend the MCS calculations to include the VDF's. No VDF calculations have yet been done using the 3T or BM method although such techniques have already been used to calculate speed distribution functions [16]. Here the velocity distributions are computed by intensive MCS calculations on a supercomputer.

COMPUTATION OF TRANSPORT PROPERTIES

The starting point for any theoretical calculation of the transport coefficients is the assumption of a realistic interaction potential between the colliding particles. The range of internuclear separations probed by gaseous-ion-transport data extends from the long-range, inverse-fourth-power, induced dipole-polarization-potential region to the short-range-repulsive region at a few atomic units.

The interaction potential of the Na^+-Ne system is relatively well known, and the interaction potentials derived from both ion-beam and swarm methods have yielded transport coefficients in excellent to good agreement with experimental data [17]. Both colliding species are closed-shell atomic structures with spherical symmetry and no fine-structure splitting. They have the same electronic configurations $(1s^2 2s^2 2p^6 \, ^1S_0)$, but because of the additional nuclear charge on the Na^+ ion, their electronic wave functions are not identical, so that quantum-mechanical exchange forces need not be considered except in the very-low-energy range below that probed by gaseous-ion-transport data measured at room temperature. Because of these naturally occurring simplifications, this interaction is conducive for both *ab initio* as well as semiempirical calculations.

Of the more refined interaction potentials proposed for Na^+-Ne in the last few years, among the most accurate appears to be the KMV potential given in the functional form [5]

$$V(r) = V_0[A_1 \exp(-a_1 r/\rho) - B_1 \exp(-b_1 r/\rho)]$$
$$-F[C_4/r^4 + (C_{6ind} + C_{6disp})/r^6$$
$$+ (C_{8ind} + C_{8disp})/r^8] \qquad (2)$$

with

$$F = \begin{cases} 1 & \text{for } r > 1.28 r_{min} \\ \exp[-(1.28 r_{min}/r - 1)^2] & \text{otherwise .} \end{cases} \qquad (3)$$

In atomic units, the parameters in Eqs. (2) and (3) are $V_0 = 0.5646$, $A_1 = 146.98$, $a_1 = 1.5024$, $B_1 = 70.198$, $b_1 = 1.4041$, $\rho = 0.7607$, $C_4 = 1.3315$, $C_{6ind} = 3.74$, $C_{6disp} = 3.199$, $C_{8ind} = 17.135$, $C_{8disp} = 34.16$, and $r_{min} = 4.70$.

The KMV potential was used as input to our MCS, 3T, and BM calculation procedures to compute the mobility and diffusion coefficients for Na^+ in Ne at room temperature. The calculational methods have been previously described [1,2,16]. As in the case for the K^+-Ar interaction [2], a classical treatment for the present ion–neutral-atom pair is adequate except in the limit of very-small-angle scattering. Small-angle scattering is handled by finding a correction to the total scattering cross section which gives for a fixed cutoff angle $\chi_{min} = 0.15$ rad the same contribution to the momentum-transfer cross section as that obtained from all collisions with $|\chi| < |\chi_{min}|$ [1]. Several important enhancements in the present MCS procedure compared to more traditional simulation methods are worth noting.

TABLE I. MCS calculated values of K_0, D_T/K and $D_T^{(r)}$.

E/N (Td)	T_{eff} (K)	K_0 (cm²/V s)	D_T/K (mV)	Standard Deviation of D_T/K		$D_T^{(r)}$
				(mV)	(%)	
5	304.7	8.17	26.0	0.2	0.8	0.999
10	335.3	8.31	28.3	0.1	0.4	1.021
15	391.4	8.57	32.3	0.1	0.4	1.058
20	479.3	8.88	38.6	0.1	0.3	1.118
25	602.9	9.18	47.9	0.2	0.4	1.207
25	603.2	9.19	47.6	0.3	0.7	1.202
30	763.5	9.44	58.2	0.3	0.4	1.268
35	946.2	9.54	71.6	0.2	0.3	1.342
40	1 152.6	9.58	85.6	0.5	0.6	1.383
45	1 373.3	9.55	100.0	0.6	0.6	1.398
50	1 612.1	9.50	115.6	0.9	0.8	1.404
55	1 866.2	9.43	131.6	1.3	1.0	1.395
60	2 147	9.39	149.2	1.2	0.8	1.389
70	2 700	9.17	184.9	1.6	0.9	1.350
80	3 287	8.95	223	2.0	0.9	1.302
100	4 534	8.52	299	4.6	1.5	1.179
120	5 888	8.16	386	6.1	1.6	1.093
140	7 332	7.84	477	10.7	2.2	1.011
170	9 600	7.43	619	14.9	2.4	0.904
200	12 094	7.11	775	22.2	2.9	0.828

(i) The present calculations account for the variation of collision frequency with the relative velocity of the colliding particles, and are therefore not dependent on the validity of either a constant-mean-free-path or a constant-mean-free-time model (compare, e.g., [18]).

(ii) The calculations also allow for the fact that the ion-atom scattering is not isotropic in the center-of-mass frame (compare, e.g., [19]). We compute the scattering angle with an elaborate Gauss-Mehler 32-point quadrature, which was chosen because of its suitability even

TABLE II. 3T calculated values of K_0, ND_T, $D_T^{(r)}$, ND_L, and $D_L^{(r)}$.

E/N (Td)	T_{eff} (K)	K_0 (cm²/V s)	ND_T (10^{20}/m s)	$D_T^{(r)}$	ND_L (10^{20}/m s)	$D_L^{(r)}$
10.07	339.0	8.321	6.394	1.022	7.306	1.167
10.65	344.1	8.347	6.497	1.025	7.537	1.189
11.25	349.9	8.375	6.614	1.029	7.800	1.214
11.89	356.3	8.406	6.747	1.034	8.101	1.241
12.55	363.6	8.441	6.898	1.039	8.443	1.272
13.25	371.7	8.476	7.062	1.045	8.795	1.301
13.99	380.8	8.517	7.249	1.051	9.208	1.335
14.75	391.1	8.561	7.463	1.059	9.686	1.375
15.55	402.7	8.608	7.703	1.068	10.222	1.417
16.39	415.6	8.659	7.972	1.078	10.823	1.463
17.26	430.1	8.712	8.273	1.089	11.499	1.513
18.17	446.6	8.780	8.653	1.105	12.536	1.601
19.10	464.7	8.845	9.048	1.120	13.425	1.662
20.10	484.5	8.891	9.440	1.133	13.897	1.668
21.15	506.8	8.940	9.890	1.148	14.722	1.709
22.26	531.6	8.987	10.378	1.163	15.580	1.746
23.41	559.2	9.034	10.909	1.178	16.517	1.783
24.61	589.9	9.086	11.494	1.193	17.609	1.828
25.85	624.2	9.142	12.143	1.209	18.926	1.884
27.15	662.5	9.204	12.872	1.226	20.51	1.953
28.50	705.5	9.269	13.692	1.245	22.35	2.031
29.91	753.5	9.337	14.615	1.265	24.39	2.111
31.41	807.4	9.404	15.652	1.287	26.54	2.182
33.00	867.9	9.468	16.810	1.309	28.71	2.237
34.69	935.9	9.526	18.100	1.332	30.85	2.271
36.52	1012.5	9.577	19.530	1.354	32.92	2.282
38.50	1099.0	9.619	21.11	1.374	34.90	2.272
40.66	1196.9	9.648	22.86	1.392	36.84	2.244
43.03	1307.8	9.665	24.78	1.407	38.76	2.201
45.63	1433.6	9.665	26.89	1.417	40.72	2.146
48.49	1576.0	9.648	29.20	1.422	42.77	2.083
51.65	1737.3	9.612	31.73	1.422	44.94	2.013
55.14	1919.5	9.556	34.50	1.415	47.29	1.940
59.03	2124	9.473	37.47	1.402	50.00	1.870
63.29	2356	9.380	40.76	1.383	52.79	1.792
67.96	2621	9.280	44.41	1.361	55.65	1.705
73.10	2921	9.169	48.45	1.335	58.67	1.616
78.73	3261	9.047	52.89	1.304	61.95	1.528
84.94	3644	8.911	57.77	1.270	65.58	1.442
91.77	4075	8.764	63.11	1.233	69.63	1.360
99.28	4561	8.606	68.95	1.192	74.18	1.283
107.52	5106	8.439	75.34	1.150	79.31	1.211
116.56	5719	8.266	82.33	1.106	85.07	1.143
126.47	6411	8.090	89.76	1.059	91.07	1.075
137.30	7183	7.908	98.12	1.015	98.66	1.021
149.13	8052	7.726	107.51	0.973	107.83	0.976
162.04	9023	7.543	117.63	0.931	116.22	0.920
176.10	10118	7.363	128.73	0.889	126.54	0.874
191.40	11347	7.187	140.95	0.849	138.12	0.832
208.03	12729	7.013	154.43	0.810	151.14	0.793
226.06	14280	6.845	169.30	0.774	165.77	0.758
245.60	16024	6.682	185.75	0.739	182.19	0.725
266.74	17984	6.524	203.96	0.707	200.67	0.696

when the integrand becomes unbounded at one end of the integration limit. We have utilized the high-capacity random-access memory of the supercomputer to maintain a large, rapidly accessible, table of scattering angles, $\chi(\epsilon, b)$, as a function of impact parameter b and collision energy ϵ. Typically, this table contains 240 ϵ values and 400 b values.

(iii) Full provision is allowed for the random thermal motion of the buffer-gas particles, as opposed to a cold-gas model where the buffer particles have fixed positions in space (compare, e.g., [20]). Mason and McDaniel [6(b)] have emphasized that the cold-gas limit of transport properties is not equivalent to the high E/N limit, as a third energy scale, namely, the interaction potential energy $V(r)$, is also involved in the theoretical considerations.

(iv) To reduce the propagation of errors, double-precision arithmetic with a precision of 1 in 10^{17} was employed in calculating the $\chi(\epsilon, b)$ table. Error propagation was discernibly detectable in the near-classical-orbiting region, where $\chi(\epsilon, b)$ changes rapidly.

The detailed results of our transport calculations are given in Tables I and II. Figure 1 shows a comparison of the calculated mobilities with experimental values of Ellis *et al.* [21] and Iinuma *et al.* [22], which have a claimed accuracy of $\pm 2\%$ and $\pm 2.5\%$, respectively. Generally, a standard deviation of less than 1% is attained in the MCS mobilities and the 3T calculations have converged within 0.1%. In the region from 20 to 50 Td, the 3T mobilities had not completely stabilized by the eighth approximation, which is the highest level of approximation the computer program had been designed to permit. We therefore supplemented these calculations with BM calculations that could be carried to higher levels of approximation. As can be seen in Fig. 1, the 3T and BM results agree within the estimated combined error of 0.5%, thus demonstrating that the 3T calculations had, in fact, been adequate. Closer examination of the seventh and eighth approximations of the 3T mobilities revealed that they
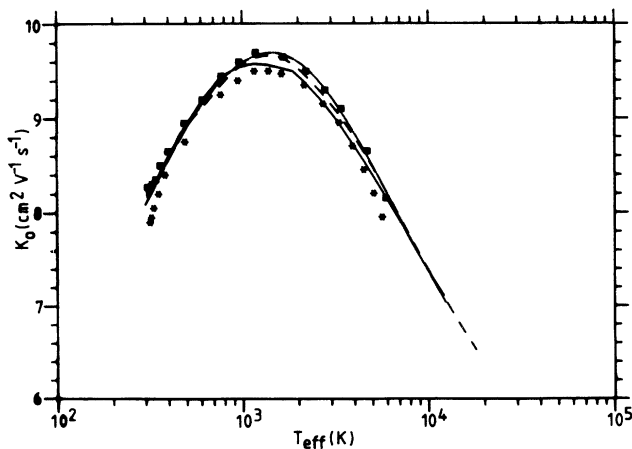

FIG. 2. Comparison of theoretical (3T, —— —— ——; BM ——·——·——·—— ; GER derived values using mobility data of Iinuma *et al.* [22], asterisks), MCS (——), and experimental (Hogan and Ong [25], squares) transverse-diffusion data in the form of reduced transverse-diffusion coefficient to mobility ratios on the same E/N (the ratio of electric field to neutral particle number density) scale.

tend to oscillate around the BM values (presumably correct) without deviating by more than 1%.

It should be noted that the horizontal axis in Fig. 1 is the effective temperature defined by

$$T_{\text{eff}}(T, E/N) = T + \frac{1}{3k_B} MN_0^2 [K_0(T, E/N)]^2 (E/N)^2 \quad (4)$$

where M is the neutral-atom mass, N_0 is Loschmidt's number, $K_0(T, E/N)$ is the reduced mobility measured at absolute temperature T and at a specified E/N value, and k_B is Boltzmann's constant. This way of presenting the data was chosen in order to adjust for slight differences in the temperatures of the various data sets. The MCS data were calculated at the gas temperature 295 K, and the 3T and BM data at 298 K. Since the experimental data were collected over a small range of temperatures, the average temperature of 300 K for the data of Ellis *et al.* and 313 K for the data of Iinuma *et al.* were assumed. The effective temperature scaling rule [6(c)] combining the

FIG. 1. Comparison of theoretical (3T, —— —— ——; BM, ——·——·——·——), MCS (——), and experimental (Iinuma *et al.* [22], asterisks; Ellis *et al.* [21], squares) mobility data in the form of reduced mobilities.

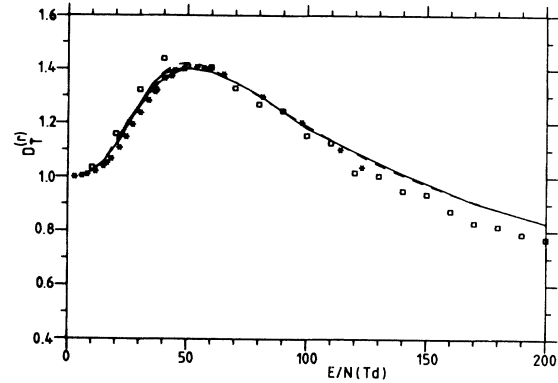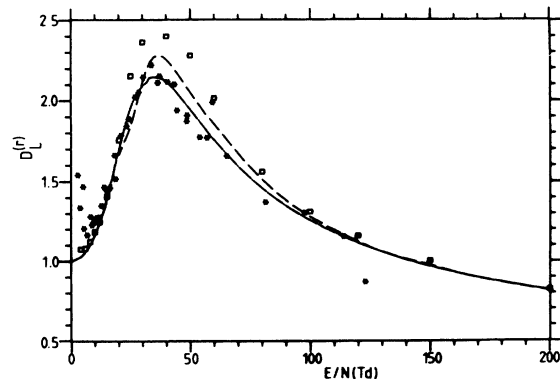FIG. 3. Comparison of theoretical (3T, —— —— ——; BM ——·——·——·——) and experimental (Iinuma *et al.* [22], asterisks; Ellis *et al.* [26], squares) longitudinal-diffusion data in the form of reduced longitudinal-diffusion coefficient to mobility ratios on the same E/N (as defined in Fig. 2) scale.

effects of T and E/N into a single parameter has recently been reaffirmed by experiment [23].

For all of the results plotted in Fig. 1, the mobility reaches a maximum value at about 45 Td (1 Td$=10^{-21}$ Vm^2), corresponding to $T_{\text{eff}} \cong 1300$ K. This peaking of the mobility curve occurs when there is a partial cancellation of the deflections produced by the attractive and repulsive parts of $V(r)$. The maximum thus corresponds to the region of near-glory scattering, where the ions are only slightly scattered by the neutral atoms, their momentum-transfer cross section is small, and they experience reduced resistance to their motion. At the peak mobility, the average center-of-mass collision energy is 0.0067 hartree, and the impact parameter for glory scattering corresponding to this energy is about 6.7 Bohr radii. (Glory scattering is a quantum-mechanical effect at small scattering angles that occurs when scattering by the attractive and repulsive parts of the potential approximately cancel [24].)

Diffusion data shown in Figs. 2 and 3 are presented in a reduced form, given by

$$D_{T,L}^{(r)} = (e/k_B T_{\text{pol}})(D_{T,L}/K) , \qquad (5)$$

where

$$T_{\text{pol}} = T + M(N_0 K_{\text{pol}} E/N)^2 / 3k_B . \qquad (6)$$

Here $D_T^{(r)}$ and $D_L^{(r)}$ are dimensionless ratios, e is the electronic charge, D_T/K and D_L/K are the ratios, respectively, of the transverse- and longitudinal-diffusion coefficients to mobility, and T_{pol} is the ion temperature in the polarization limit. This definition of $D_{T,L}^{(r)}$ treats the ratio $D_{T,L}/K$ as a single entity, rather than as two separate quantities, and should properly be referred to as the reduced (transverse, longitudinal) diffusion coefficient to mobility ratio. Equations (5) and (6) are similar to ones proposed earlier [6(d)] but have the important advantage that they can be obtained directly from known constants and the value of $D_{T,L}/K$, without requiring independent knowledge of K. These reduced ratios remove the first-order dependence on temperature of $D_{T,L}/K$ and amplify the details of the variation of the diffusion coefficients with E/N. Their use also gives approximately linear effects from experimental errors throughout the range of E/N, instead of rapidly growing effects at low E/N as with a previously used reduction scheme [1,4]. For plotting values of $ND_{T,L}$, the corresponding $D_{T,L}^{(r)}$ values have been calculated using literature values of mobility.

FIG. 4. Velocity distribution functions (in arbitrary units) along different axes, without restriction on the other components of ion velocity for (a) $E/N = 5$ Td, (b) $E/N = 37.5$ Td, (c) $E/N = 100$ Td, and (d) $E/N = 200$ Td. [$f(v_x)$, ———; $f(v_y)$, asterisks; $f(v_{45})$, ——— ——— ———; $f(v_{45e})$, triangles; $f(v_z)$, ——— · ——— · ——— · ———].

Our transverse-diffusion results are compared against the experimental D_T/K values of Hogan and Ong [25] in Fig. 2. To our knowledge, these are the only experimental data available. Also shown are the diffusion coefficients obtained from the generalized Einstein relationships (GER) [6(e)] calculated using the experimental mobility values of Iinuma et al. [22]. The data sets all show a maximum, for the same physical reasons as there is a mobility maximum. The MCS values for the transverse-diffusion coefficients have a standard deviation of less than 2%, while the 3T values have generally converged within 0.25%. BM calculations have again been used to supplement the 3T values between 20 and 50 Td. The errors for the experimental values of D_T/K are ±3%. Keeping these errors in mind, in addition to the smaller errors of the mobilities used to determine the GER and calculated values of $D_T^{(r)}$, we see again that the calculated results agree quite well with experiment and with each other.

The calculated values of the longitudinal-diffusion coefficients are compared with the experimentally determined values of Iinuma et al. [22] and Ellis et al. [26] in Fig. 3. Since ND_L values were measured directly rather than as values of D_L/K, we used the mobilities measured by the same groups [22,21] to compute the values of $D_L^{(r)}$ shown in Fig. 3. This introduces very little additional error considering the estimated errors of ±5% for the data of Ellis et al. [26], and of up to ±18% at low and high E/N and ±7% at intermediate E/N for the data of Iinuma et al. [22].

MCS results are not shown in Fig. 3 because it was found that the standard deviation of the longitudinal-diffusion coefficients was unacceptably large. In general, the 3T and BM calculations of ND_L converged within the requested 0.25% accuracy. The differences at E/N values between 35 and 90 Td are due to a lack of convergence in the 3T calculations. The poor convergence of the 3T results near the maximum compared with the much better convergence of the BM values, which was also present in the K and $D_T^{(r)}$ values to a somewhat lesser extent, is perhaps an indication of the occurrence of partial ion runaway [16]. The converged BM results can be seen to agree with the experimental values throughout the range of E/N, keeping in mind the somewhat large experimental errors.

The general agreement between the calculated and experimental values of the transport properties confirms that the KMV potential represents fairly closely the true Na^+-Ne interaction potential. This conclusion provides us the necessary confidence for the use of the KMV potential in the more intensive second stage of the present calculations in which the velocity distribution functions are determined. The fact that the mobility and transverse-diffusion data at high E/N are systematically slightly higher than the calculated values may indicate that the repulsive region of the KMV potential is somewhat too soft. More accurate longitudinal-diffusion data at high E/N are needed to clarify this point.

A second conclusion we draw from the generally good agreements shown in Figs. 1–3 is that the different sets

TABLE III. Shape parameters of velocity distribution functions along various axes.

VDF	Peak (m/s)	Skewness	Excess
	$E/N = 5$ Td		
$f(v_x)$	0	0.001	-0.003
$f(v_y)$	0	0.000	-0.022
$f(v_z)$	110	0.039	-0.003
$f(v_{45})$	100	0.022	-0.011
$f(v_{45e})$	100	0.024	-0.008
	$E/N = 37.5$ Td		
$f(v_x)$	0	-0.003	0.767
$f(v_y)$	0	0.008	0.769
$f(v_z)$	720	0.690	0.687
$f(v_{45})$	500	0.579	0.707
$f(v_{45e})$	600	0.308	0.345
	$E/N = 100$ Td		
$f(v_x)$	0	-0.004	0.800
$f(v_y)$	0	-0.006	0.842
$f(v_z)$	1750	0.635	0.362
$f(v_{45})$	1120	0.538	0.500
$f(v_{45e})$	1400	0.300	0.256
	$E/N = 200$ Td		
$f(v_x)$	0	0.007	0.795
$f(v_y)$	0	-0.001	0.784
$f(v_z)$	2950	0.566	0.103
$f(v_{45})$	2000	0.512	0.432
$f(v_{45e})$	2300	0.275	0.201

of experimental mobility and diffusion values are consistent within their claimed accuracies, with the partial exception of longitudinal diffusion. Finally, the excellent agreement between the calculated values, found whenever the calculations have converged, validates the computer programs used for the MCS, 3T, and BM procedures.

VELOCITY DISTRIBUTION FUNCTIONS

There is as yet no general, analytical solution to the Boltzmann equation. However, with adequate computer power and realistic input parameters, the MCS method is a phenomenologically straightforward and practical alternative approach to determining the velocity distribution function. We determined this distribution by running the MCS computer program and, at the end of each ion free flight, incrementing the appropriate velocity bin(s) by the duration(s) the ion spent in each bin's range. As in most previous simulations (e.g., [9,14,20]), Cartesian coordinates are used to describe the three-dimensional velocity space. Although this forsakes the cylindrical symmetry of the problem, the Cartesian system continues to be used because of its computational simplicity and ease of visualization.

VDF's have been calculated for several sampling conditions. Figures 4(a)–4(d) show the various VDF's of Na^+ in room temperature (295 K) neon along different directions at $E/N = 5$, 37.5, 100 and 200 Td, respectively. Here v_z is the velocity component along the electric-field direction, while v_x and v_y are orthogonal to v_z and to each other. $f(v_x)$, $f(v_y)$, and $f(v_z)$ are the distribution functions of the three components of the velocity along the respective Cartesian axes, as logged by the MCS program. They represent the sum of the contributions from all ions to the given velocity component, regardless of the other velocity components. By virtue of the cylindrical symmetry, $f(v_x)$ and $f(v_y)$ are identical within the statistical uncertainties (about $\pm 1\%$) of the calculation.

In a similar manner, the $f(v_{45})$ and $f(v_{45e})$ functions both represent the total ionic contribution to the VDF along the oblique line in the $v_x - v_z$ plane but inclined at 45° to the v_x and v_z axes. They differ in that $f(v_{45})$ was calculated directly from MCS data logging, whereas $f(v_{45e})$ was obtained by eliciting it from a cross product of $f(v_x)$ and $f(v_z)$. Once an ion is placed in a particular velocity bin, the only information available is the range of the bin, so it is understandable that $f(v_{45e})$ is more
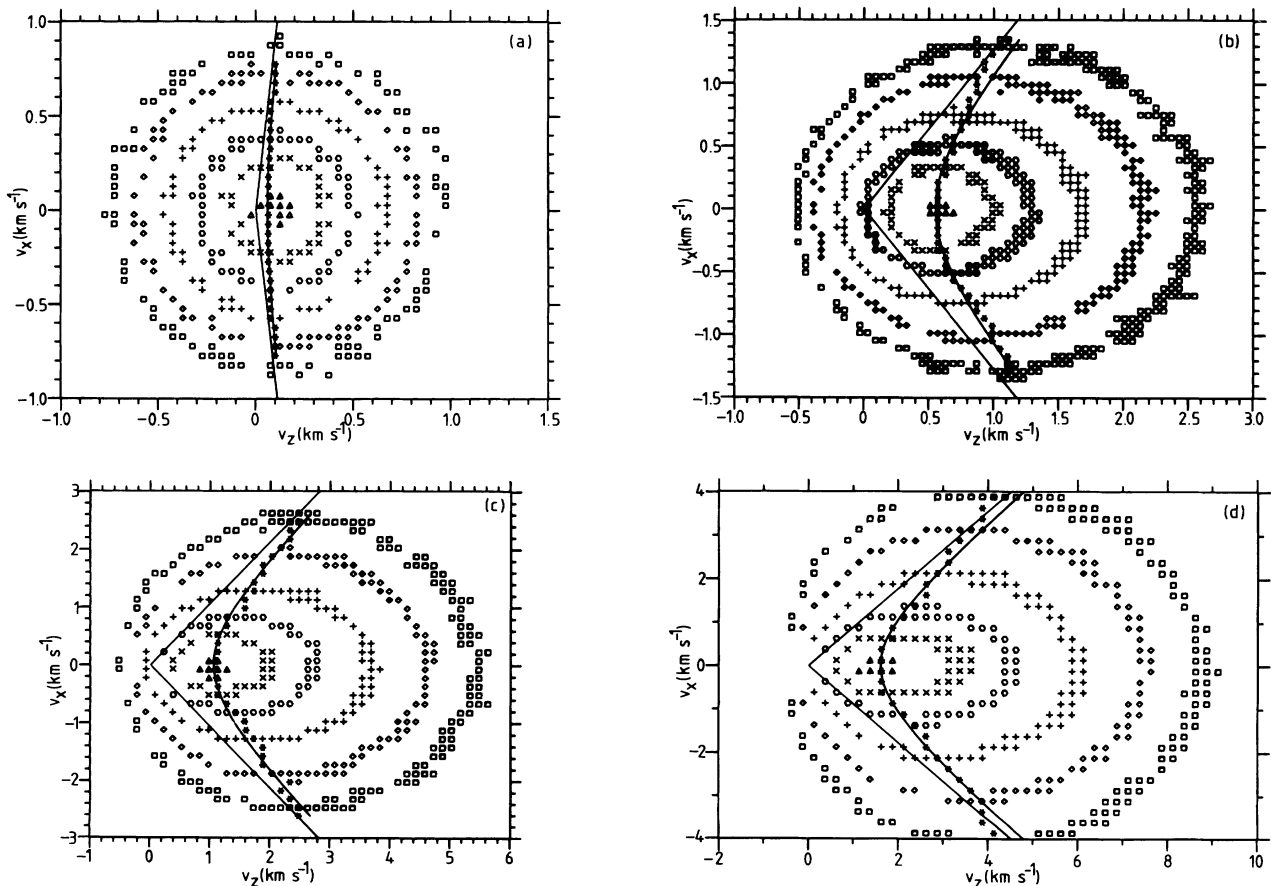

FIG. 5. Velocity contours in the plane containing the v_x and v_z axes for (a) $E/N = 5$ Td, (b) $E/N = 37.5$ Td, (c) $E/N = 100$ Td, and (d) $E/N = 200$ Td. Squares, 4%, diamonds, 10%, pluses, 25%, hexagons, 50%, crosses, 75%, and triangles, 100% of the highest contour. Asterisks show the peaks read from the MCS calculations. The hyperbola and its asymptotes fitting these peaks are also shown.

jagged than $f(v_{45})$, since it is deduced from reduced information. Nevertheless, a substantial difference still exists between $f(v_{45})$ and $f(v_{45e})$ at each value of E/N other than 5 Td. The significance of this discrepancy is that a non-negligible correlation exists between the axial and transverse motions of the ions. Had there been no such correlation, $f(v_{45})$ and $f(v_{45e})$ should have agreed within statistical uncertainties. Qualitatively, as E/N increases, the $f(v_{45e})$ curve becomes progressively more displaced to the direction of higher velocity than $f(v_{45})$, indicating the increasing correlation of v_x and v_z. Physically it may be interpreted that ions moving rapidly in the v_z direction will have the high velocity regions of the $f(v_x)$ and $f(v_y)$ distributions enhanced. A correlation like this has long been suspected [9] but never rigorously proven. However, the results of our MCS calculations should be sufficiently convincing.

An immediate consequence of the correlation is that it would not be correct to express the combined velocity distribution function of the ions as the product of three separable functions, such as

$$F(v_x, v_y, v_z) = f_x(v_x) f_y(v_y) f_z(v_z) , \tag{7}$$

as has often been assumed [20]. For simplicity, throughout this paper we have dropped the suffixes after the f's with the implicit understanding that in general $f_x = f_y \neq f_z$.

In principle, all of the distributions presented here can be directly obtained from experimental measurements, except $f(v_{45e})$. With a sufficiently accurate LIF experiment, it should even be possible to confirm the distinction between $f(v_{45})$ and $f(v_{45e})$ directly. The VDF measured with the laser pointed at 45° to the z axis would measure $f(v_{45})$, while the $f(v_{45e})$ can be deduced analytically from two separate measurements with the laser along and perpendicular to the z axis.

To facilitate comparison with future experimental results, the velocity of the peak, skewness (δ), and excess kurtosis (η) of the various curves are presented in Table III. The last two quantities are defined by

$$\delta = \langle (v_z - \langle v_z \rangle)^3 \rangle / \langle (v_z - \langle v_z \rangle)^2 \rangle^{3/2} \tag{8}$$
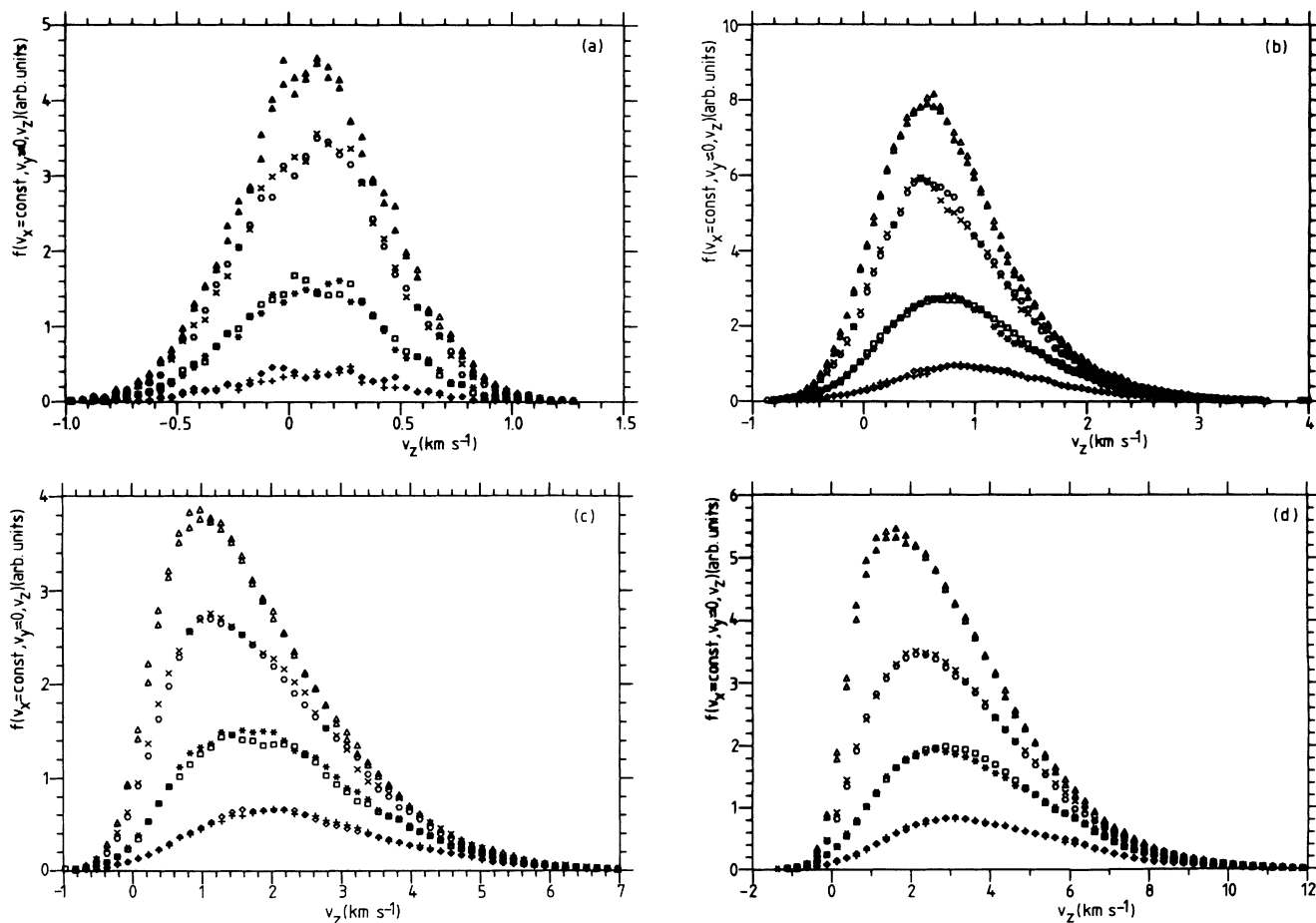

FIG. 6. Sample profiles of the velocity contours of Fig. 5 for (a) $E/N = 5$ Td: $v_x = 0$, triangles; $v_x = \pm 225$ m/s, hexagons and crosses; $v_x = \pm 475$ m/s, squares and asterisks; $v_x = \pm 725$ m/s, diamonds and pluses; (b) $E/N = 37.5$ Td: $v_x = 0$, triangles; $v_x = \pm 330$ m/s, hexagons and crosses; $v_x = \pm 630$ m/s, squares and asterisks; $v_x = \pm 990$ m/s, diamonds and pluses; (c) $E/N = 100$ Td: $v_x = 0$, triangles; $v_x = \pm 525$ m/s, hexagons and crosses; $v_x = \pm 975$ m/s, squares and asterisks; $v_x = \pm 1575$ m/s, diamonds and pluses, and (d) $E/N = 200$ Td: $v_x = 0$, triangles; $v_x = \pm 875$ m/s, hexagons and crosses; $v_x = \pm 1625$ m/s, squares and asterisks; $v_x = \pm 2625$ m/s, diamonds and pluses.

TABLE IV. Peaks of $f(v_x = \text{const}, v_y = 0, v_z)$ and their deviations from the respective fitted hyperbolic (hyp. fit) equation.

v_x (m/s)	v_z (m/s) MCS	hyp. fit	Absolute % difference
	$E/N = 5$ Td, $a = 60$ m/s, $b = 540$ m/s, $a/b = 0.11$		
−775	100	104.95	4.72
−725	100	100.44	0.44
−675	100	96.05	4.12
−625	100	91.77	8.96
−575	75	87.65	14.43
−525	75	83.68	10.38
−475	75	79.91	6.14
−425	75	76.35	1.77
−375	75	73.05	2.67
−325	70	70.03	0.04
−275	65	67.33	3.46
−225	65	65.00	0.00
−175	65	63.07	3.06
−125	65	61.59	5.54
−75	65	60.58	7.30
−25	65	60.06	8.22
25	65	60.06	8.22
75	65	60.58	7.30
125	65	61.59	5.54
175	65	63.07	3.06
225	70	65.00	7.69
275	70	67.33	3.96
325	75	70.03	7.10
375	75	73.05	2.67
425	75	76.35	1.77
475	75	79.91	6.14
525	75	83.68	10.38
575	75	87.65	14.43
625	100	91.77	8.96
675	100	96.05	4.12
725	100	100.44	0.44
775	100	104.95	4.72
Average absolute % difference of v_z			5.28
	$E/N = 37.5$ Td, $a = 550$ m/s, $b = 700$ m/s, $a/b = 0.79$		
−1290	1110	1153	3.74
−1230	1110	1112	0.18
−1170	1110	1071	3.62
−1110	1050	1031	1.83
−1050	990	992	0.15
−990	990	953	3.92
−930	990	915	8.25
−870	930	877	6.00
−810	870	841	3.43
−750	870	806	7.93
−690	810	772	4.88
−630	750	740	1.36
−570	690	709	2.72
−510	690	680	1.40
−450	630	654	3.65
−390	630	630	0.06
−330	570	608	6.26
−270	570	589	3.31
−210	570	574	0.73
−150	570	562	1.34
−90	570	555	2.79

TABLE IV. (*Continued*).

v_x (m/s)	v_z (m/s) MCS	hyp. fit	Absolute % difference
$E/N = 37.5$ Td, $a = 550$ m/s, $b = 700$ m/s, $a/b = 0.79$			
-30	570	551	3.54
30	570	551	3.54
90	570	555	2.79
150	570	562	1.34
210	570	574	0.73
270	630	589	6.87
330	630	608	3.61
390	630	630	0.06
450	690	654	5.53
510	690	680	1.40
570	690	709	2.72
630	750	740	1.36
690	750	772	2.89
750	810	806	0.49
810	810	841	3.70
870	810	877	7.68
930	870	915	4.87
990	870	953	8.68
1050	870	992	12.26
1110	930	1031	9.80
1170	930	1071	13.19
1230	990	1112	10.97
1290	1050	1153	8.95
1350	1110	1195	7.10
Average absolute % difference of v_z			4.26
$E/N = 100$ Td, $a = 1050$ m/s, $b = 1120$ m/s, $a/b = 0.94$			
-2625	2475	2676	7.50
-2475	2475	2547	2.82
-2320	2325	2415	3.73
-2175	2175	2294	5.17
-2025	2325	2169	7.17
-1875	2025	2048	1.10
-1725	1875	1928	2.76
-1575	1875	1812	3.49
-1425	1875	1699	10.35
-1275	1725	1591	8.42
-1125	1600	1488	7.51
-975	1575	1392	13.14
-825	1425	1304	9.27
-675	1275	1226	4.00
-525	1125	1160	2.99
-375	1125	1107	1.60
-225	1100	1071	2.71
-75	1075	1052	2.15
75	1075	1052	2.15
225	1125	1071	5.04
375	1125	1107	1.60
525	1125	1160	2.99
675	1275	1226	4.00
825	1275	1304	2.23
975	1575	1392	13.14
1125	1575	1488	5.83
1275	1725	1591	8.42
1425	1725	1699	1.52
1575	1875	1812	3.49
1725	1875	1928	2.76
1875	2025	2048	1.10

TABLE IV. (Continued).

v_x (m/s)	v_z (m/s) MCS	hyp. fit	Absolute % difference
	$E/N = 100$ Td, $a = 1050$ m/s, $b = 1120$ m/s, $a/b = 0.94$		
2025	2175	2169	0.26
2175	2325	2294	1.37
2325	2325	2419	3.90
2475	2475	2547	2.82
2625	2475	2676	7.50
Average absolute % difference of v_z			4.61
	$E/N = 200$ Td, $a = 1600$ m/s, $b = 1420$ m/s, $a/b = 1.13$		
−4125	4375	4916	11.00
−3875	4125	4650	11.29
−3625	3875	4387	11.66
−3375	3875	4126	6.08
−3125	3875	3868	0.19
−2875	3625	3613	0.33
−2625	3375	3363	0.36
−2375	3125	3118	0.23
−2125	2875	2880	0.17
−1875	2625	2650	0.95
−1625	2625	2432	7.96
−1375	2375	2227	6.64
−1125	2125	2041	4.10
−875	1875	1879	0.23
−625	1625	1748	7.04
−375	1625	1655	1.80
−125	1625	1606	1.17
125	1625	1606	1.17
375	1625	1655	1.80
625	1875	1748	7.26
875	1875	1879	0.23
1125	2125	2041	4.10
1375	2375	2227	6.64
1625	2625	2432	7.96
1875	2625	2650	0.95
2125	2875	2880	0.17
2375	3125	3118	0.23
2625	3125	3363	7.07
2875	3375	3613	6.59
3125	3625	3868	6.27
3375	3875	4126	6.08
3625	3875	4387	11.66
3875	4125	4650	11.29
4125	4125	4916	16.08
Average absolute % difference of v_z			4.18

and

$$\eta = \langle (v_z - \langle v_z \rangle)^4 \rangle / \langle (v_z - \langle v_z \rangle)^2 \rangle^2 - 3 , \qquad (9)$$

and they indicate the deviations of the respective distributions from the normal distributions.

From the trend shown in Table III it is noted that at very small E/N both the skewness and excess kurtosis are nearly zero; the ion-velocity distribution is nearly isotropic and normal. As E/N increases, both the VDF's in the transverse directions remain symmetric, but the skewness of the longitudinal VDF first rises rapidly and then decays slowly towards large E/N. The same trend is also exhibited by the excess kurtosis in both the longitudinal and transverse directions. Since all the VDF's have positive excess kurtosis, it follows that for the same full width at half maximum (FWHM) they are generally taller and narrower (more leptokurtic) than the corresponding Gaussian distribution. In fact, the transverse VDF's are even more leptokurtic than the longitudinal VDF, signifying that as the ions are driven by the electric

field in one direction their velocity distributions in the perpendicular directions tend to get compressed.

Stronger evidence of the correlation of different velocity components can be seen from the various VDF contour plots in Figs. 5(a)–5(d), which show for different E/N values the equal VDF contour lines (set at 4, 10, 25, 50, 75, and 100% of the peak contour value) in the v_x-v_z plane of the velocity space. To restrict the statistics to this velocity plane, only ions whose v_y values are less than about 2% of their peak v_y value are logged. This selection ensures that any v_y correlation, even if it exists, will be negligible. The data points clustering around each contour band represent all those bins whose VDF values lie in the ±10% range of the nominal VDF band value. The scatter of the data points in each band is thus an indication of the resolution of the MCS calculations.

In order to describe the correlation more quantitatively we include in the velocity contour plots a locus of all the peaks of the $f(v_x = \text{const}, v_y \cong 0, v_z)$ at different values of v_x, and attempt to fit this locus with an analytical equation empirically. Since a linear equation is obviously not suitable, the next-higher-order equation, namely, a quadratic equation (or conic section) is chosen. Of all the possible conic sections, the hyperbolic (positive branch) equation, represented by $v_z^2/a^2 - v_x^2/b^2 = 1$, yields the best fit. Of the two parameters required, the transverse axis a can easily be read from the summit of the velocity contour. The other parameter, the conjugate axis b, is then determined to be the value that yields the least sum of the squares of the deviations of the MCS-computed peaks from the corresponding values calculated directly from the hyperbolic equation so derived.

Table IV gives the detailed positions of the MCS-calculated peaks and their deviations from the fitting hyperbola. The average deviation for each E/N hovers around 5%. Considering the simplicity of the method employed, the agreement between the hyperbolic equation and the MCS-obtained locus of the peaks is gratifying. It may thus be concluded that the hyperbola is at least a good first approximation for the given locus. The best fitting hyperbola for each E/N together with its asymptotes are also included in the contour figures. Since the strength of the $v_z v_x$ correlation varies monotonically with the displacement of the peaks, it may be surmised that this correlation strength may be given by the dimensionless ratio a/b which is the slope the asymptotes of the hyperbolas make with the v_x axis. On this basis, the correlation rises from 0.11 at $E/N = 5$ Td to 1.11 at $E/N = 200$ Td.

Figures 6(a)–6(d) show, for each E/N value studied, sample plots of $f(v_x = \text{const}, v_y \cong 0, v_z)$ for four different pairs of positive and negative values of v_x. Each of these plots is equivalent to the profile along the horizontal line of the velocity contours of Fig. 5 corresponding to the fixed value of v_x. As expected from cylindrical symmetry, there is virtually no distinction between positive and negative values of v_x. However, the peaks of the curves shift gradually towards higher v_z values as $|v_x|$ increases.

Further understanding of the correlation can be derived from a comparison of the different $f(v_z)$ shown in

Figs. 4 and 6. The first is the result of logging the contributions to the v_z velocity component of all ions irrespective of their v_y velocities, while the second specifically includes only those ions with near-zero v_y. For small E/N the two curves have essentially the same distribution showing negligible correlation of the respective velocity components. However, as E/N increases, the $f(v_z)$ curves of Fig. 4 may be regarded as a weighted average of the $f(v_z)$ curves of Figs. 6 over all v_x and v_y. From the positions of the respective peaks it may be seen that the weighting becomes progressively more biased towards the larger transverse velocities as E/N rises. The physical meaning of the general trend is that an ion with a large v_x component has a tendency to deplete its slow v_z components but does not deplete its fast v_z components quite as well. Had there been no $v_z v_x$ correlation no such discriminative depletion should be expected. For example, equal v_x profiles of the VDF contours illustrated in Fig. 4 of the paper by Penn et al. [14], calculated from the oversimplifying assumption of noncorrelation, would display peaks at the same v_z value.

CONCLUSION

The present study, based on a comparison of calculated and measured gaseous-ion-transport properties, has shown that the KMV potential for the Na$^+$-Ne interaction is a close approximation to the true potential, except perhaps at short separations. What is perhaps most needed now is additional, accurate experimental data probing the repulsive wall more carefully, so that a further refinement of the KMV potential would be appropriate.

The velocity distribution functions calculated from the KMV potential have conclusively established a sizable correlation between the respective velocity components of the ions. This correlation should not be neglected merely for the sake of mathematical expediency. It is hoped that the successful fitting of a hyperbolic curve to the VDF along the z axis for $v_y = 0$ and constant v_x can lead the way for a more quantitative description of the correlation effects. The existence of this correlation should in itself provide the stimulus for greater use of cylindrical coordinate system to describe ion-velocity space. Since the VDF strongly depends not only on the energy of collision, but also to a large extent on the ion–neutral-atom mass ratio, it may further be concluded that the correlation trends observed in this study would, at least, also be present in other ion–neutral-atom pairs with similar mass ratios.

In view of the mutual correlation of the velocity components established, it should be noted that experimental measurements of only $f(v_x)$ and $f(v_z)$ provide insufficient information for determining the overall VDF. However, it might be possible to deconvolute this VDF if additional $f(v_\Theta)$ are measured, where v_Θ is the velocity component at an angle Θ to the z axis. Alternatively, if this is not possible, then the application of a selection technique to sample data contributed from ions with a

specified transverse velocity component may be possible.

Finally, it is hoped that the velocity distribution functions computed here will provide the impetus for making an accurate measurement of them for the same ion–neutral-atom pair, if and when the necessary laser is developed.

[1] P. P. Ong and M. J. Hogan, J. Phys. B **24**, 633 (1991).

[2] M. J. Hogan and P. P. Ong, Phys. Rev. A **44**, 1597 (1991).

[3] P. P. Ong and M. J. Hogan, J. Phys. B **24**, 3193 (1991).

[4] M. J. Hogan and P. P. Ong, J. Chem. Phys. **95**, 1973 (1991).

[5] A. D. Koutselos, E. A. Mason, and L. A. Viehland, J. Chem. Phys. **93**, 7125 (1990).

[6] (a) E. A. Mason and E. W. McDaniel, *Transport Properties of Ions in Gases* (Wiley, New York, 1988); (b) *ibid.*, p. 151; (c) *ibid.*, p. 154; (d) *ibid.*, p. 288; (e) *ibid.*, p. 303.

[7] M. Mantel, G. Herre, H. Langhoff, K. Petkau, and W. Hammer, J. Phys. B **23**, 4111 (1990).

[8] L. A. Viehland, A. A. Viggiano, and E. A. Mason, J. Chem. Phys. **95**, 7286 (1991).

[9] J. H. Whealton and S. B. Woo, Phys. Rev. A **6**, 2319 (1972).

[10] T. Makabe, K. Misawa, and T. Mori, J. Phys. D **14**, 199 (1981).

[11] M. J. Hogan and P. P. Ong, J. Phys. D **19**, 2123 (1986).

[12] H. R. Skullerud and S. Holmstrøm, J. Phys. D **18**, 2375 (1985).

[13] R. A. Dressler, J. P. M. Beijers, H. Meyer, S. M. Penn, V. M. Bierbau, and S. R. Leone, J. Chem. Phys. **89**, 4707 (1988).

[14] S. M. Penn, J. P. M. Beijers, R. A. Dressler, V. M. Bierbaum, and S. R. Leone, J. Chem. Phys. **93**, 5118 (1990).

[15] L. A. Viehland and K. Kumar, Chem. Phys. **131**, 295 (1989).

[16] K. F. Ness and L. A. Viehland, Chem. Phys. **148**, 255 (1990).

[17] L. A. Viehland, Chem. Phys. **85**, 291 (1984).

[18] S. L. Lin and J. N. Bardsley, J. Chem. Phys. **66**, 435 (1977).

[19] T. Makabe, K. Misawa, and T. Mori, J. Phys. D **16**, 1893 (1983).

[20] S. Ushiroda, S. Kajita, and Y. Kondo, J. Phys. B **21**, 3303 (1988).

[21] H. W. Ellis, R. Y. Pai, E. W. McDaniel, E. A. Mason, and L. A. Viehland, At. Data Nucl. Data Tables **17**, 177 (1976).

[22] K. Iinuma, M. Takebe, Y. Satoh, and K. Seto, J. Chem. Phys. **79**, 3893 (1983).

[23] M. Takebe, M. Iizuka, K. Iinuma, and Y. Satoh, Second Australia-Japan Workshop on Gaseous Electronics and Its Applications, edited by R.W. Crompton and M. Hayashi, Tozanso, Gotemba, Japan, 1990 (unpublished), pp. 61–64.

[24] L. Bilosi, J. Chem. Phys. **53**, 3900 (1970).

[25] M. J. Hogan and P. P. Ong, J. Phys. D **23**, 1050 (1990).

[26] H. W. Ellis, E. W. McDaniel, D. L. Albritton, L. A. Viehland, S. L. Lin, and E. A. Mason, At. Data Nucl. Data Tables **22**, 179 (1978).